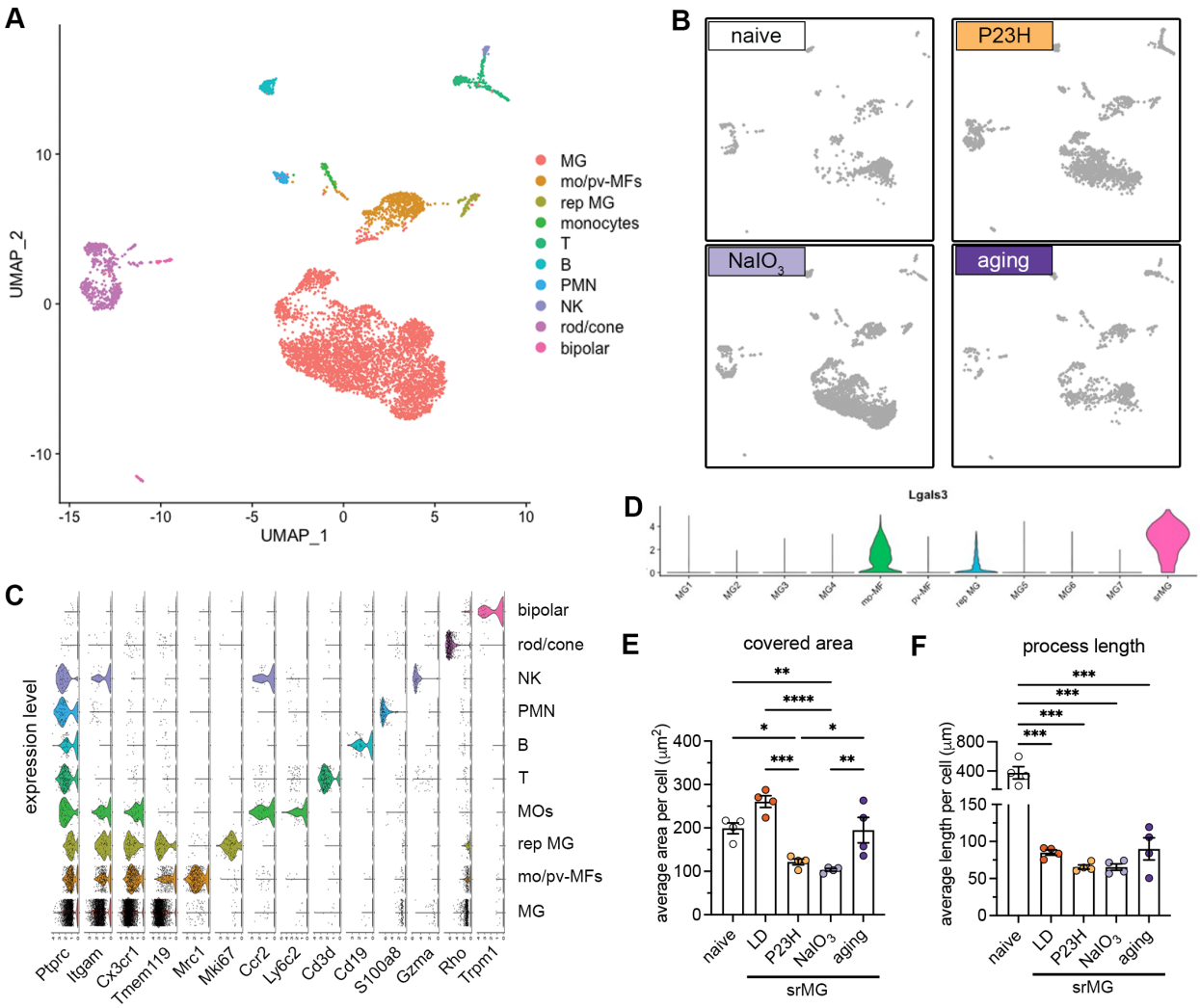

Fig. S1. scRNA-seq and morphological analysis of subretinal microglia across mouse models of outer retinal degeneration. (**A** and **B**), UMAP plots showing retinal CD45^{+} cells collected from naïve mice, $NaIO_3$ mediated RPE injury model, P23H model, and advanced aging model as indicated. (**C**) Violin plots showing marker expression for each cluster. mo-MF, monocyte-derived macrophages; pv-MF, perivascular macrophages; rep MG, replicating microglia. (**D**) Violin plots showing *Lgals3* expression across all macrophage clusters. srMG, subretinal microglia. (**E** and **F**) Quantifications of covered area and process length in naïve microglia from the inner retina and subretinal microglia from four mouse models of retinal degenerations (n=4 mice per group). *: p<0.05; **: p<0.01; ***: p<0.001 (one-way ANOVA with Tukey's post hoc test)

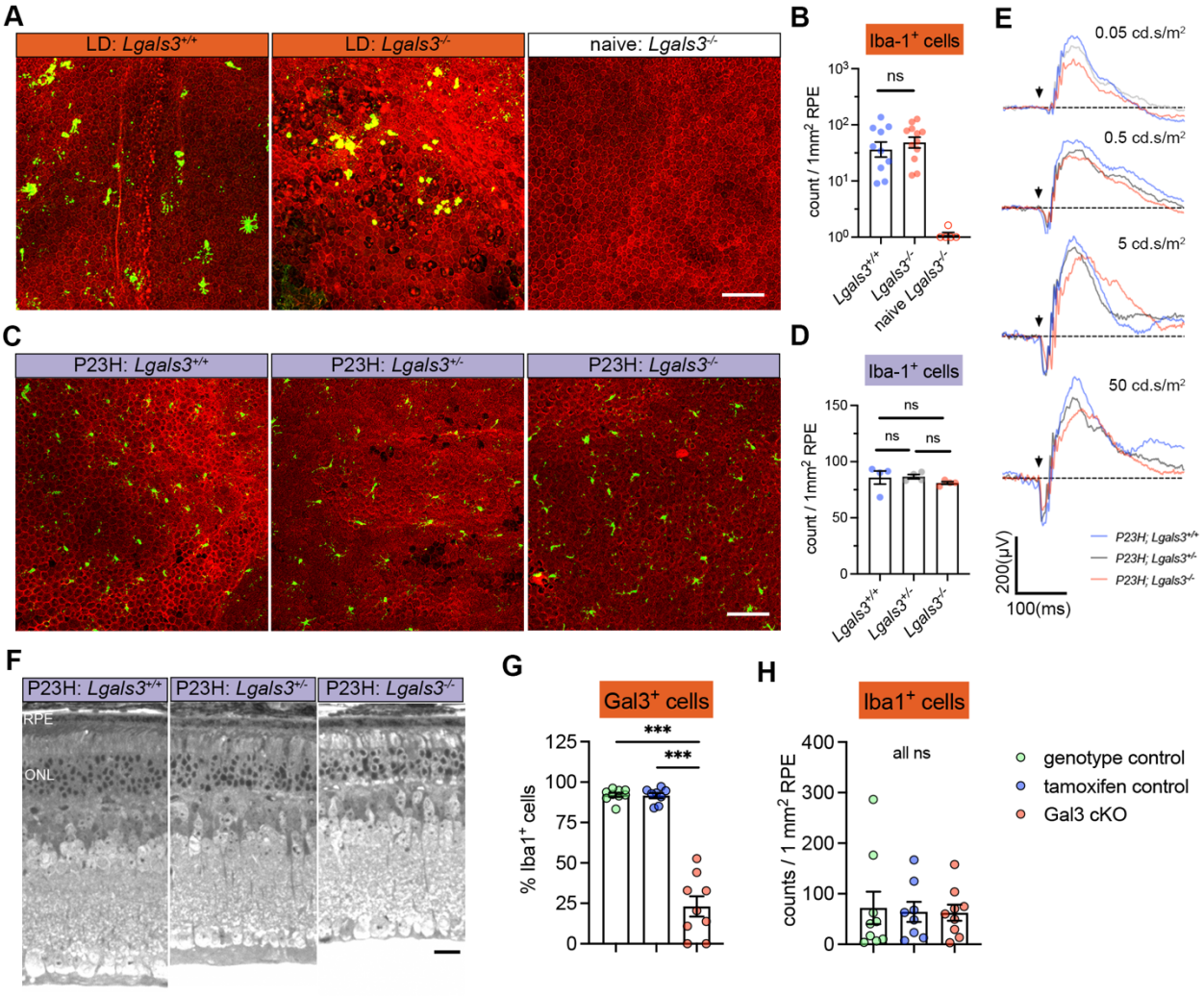

Fig. S2. Contributions of Gal3 to disease-related retinal pathology and Iba1$^+$ cell abundance in the subretinal space. (**A**) Iba1 (green) and phalloidin (red) staining in RPE flatmounts from LD-subjected mice as indicated. (**B**) Quantifications of subretinal Iba1$^+$ cells as shown in A. (**C**) Iba1 (green) and phalloidin (red) staining in RPE flatmounts from P23H mice as indicated. (**D**) Quantifications of subretinal Iba1$^+$ cells as shown in C. (**E**) Examples of ERG responses at different flash intensities as indicated. (**F**) Representative retinal cross sections of WT, *Lgal3*$^{+/-}$ and *Lgal3*$^{-/-}$ in P23H mice. (**G** and **H**) Quantifications of Gal3 depletion efficiency (G) and frequencies of subretinal Iba1$^+$ cells (H) in Gal3 cKO mice (n=9) compared with genotype control mice (n=9) and tamoxifen control (n=8). Scale bars: 100 μm. Data were collected from 2-3 independent experiments. ***: p<0.001; ns: not significant (one-way ANOVA with Tukey's post hoc test).

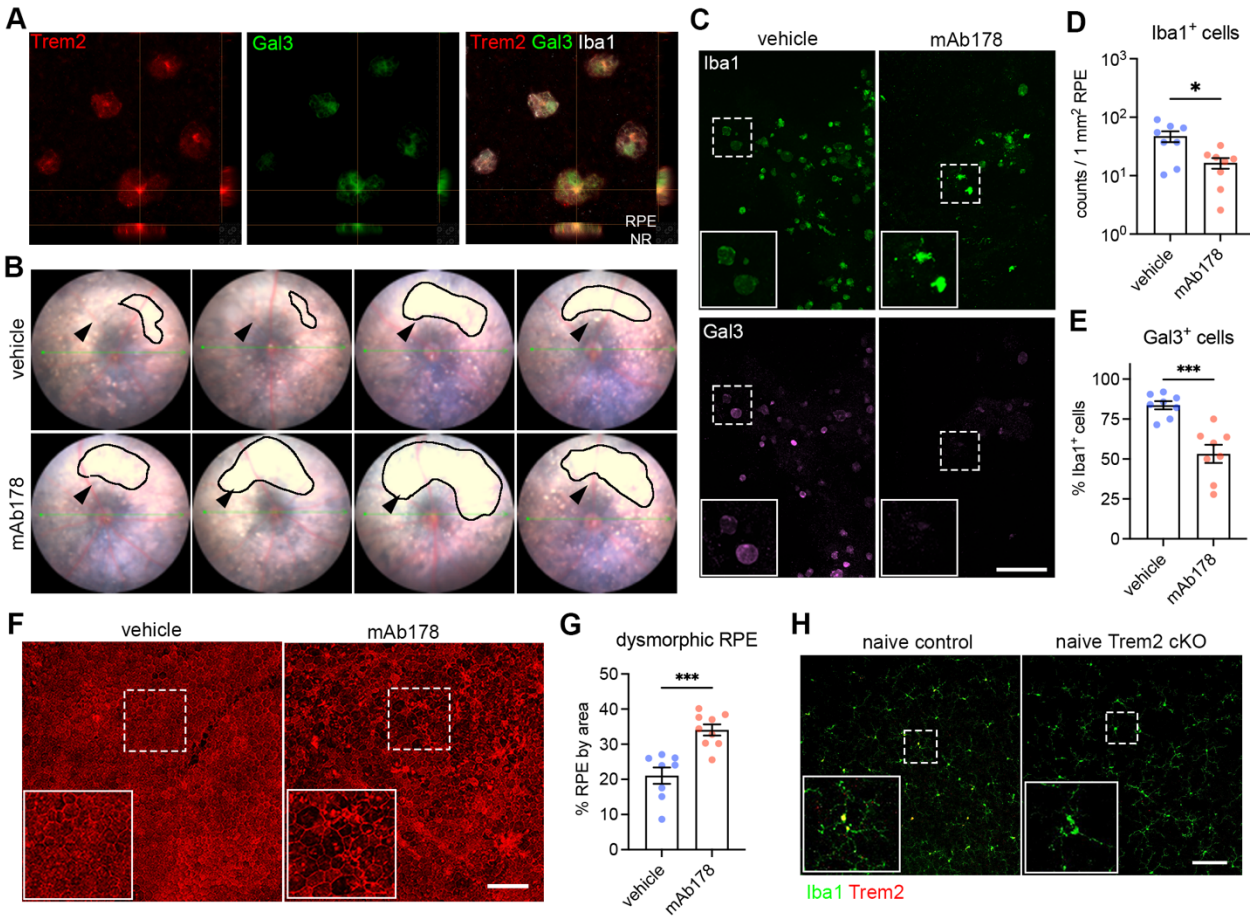

Fig. S3. Regulation by Trem2 signaling in subretinal microglia. (**A**) Split views of confocal scans showing the colocalization of Trem2 (red) and Gal3 (green) in the subretinal microglia. Lines indicate the RPE-facing and neuroretina (NR)-facing aspects as indicated. (**B**) Fundus images showing increased subretinal white lesions in anti-Trem2 mAb178 treated mice in LD as indicated by arrows. Images of 4 individual mice per group are shown. (**C**) Images of Iba1 (green) and Gal3 (magenta) staining in subretinal microglia between control and mAb178-treated mice in LD. Scale bar: 100 µm. (**D** and **E**) Quantifications of Iba1$^+$ cells and Gal3$^+$ cells between control and mAb178 (n=8 per group). (**F**) Images of phalloidin staining in RPE flatmounts from control and mAb178 treated mice in LD. Scale bar: 100µm. (**G**) Quantifications of dysmorphic RPE cells between control (n=8) and mAb178 (n=9) treated mice. (**H**) Images of Iba1 (green) and Trem2 (red) in microglia from the inner retina of naïve control and Trem2 cKO mice. Scale bar: 50µm.

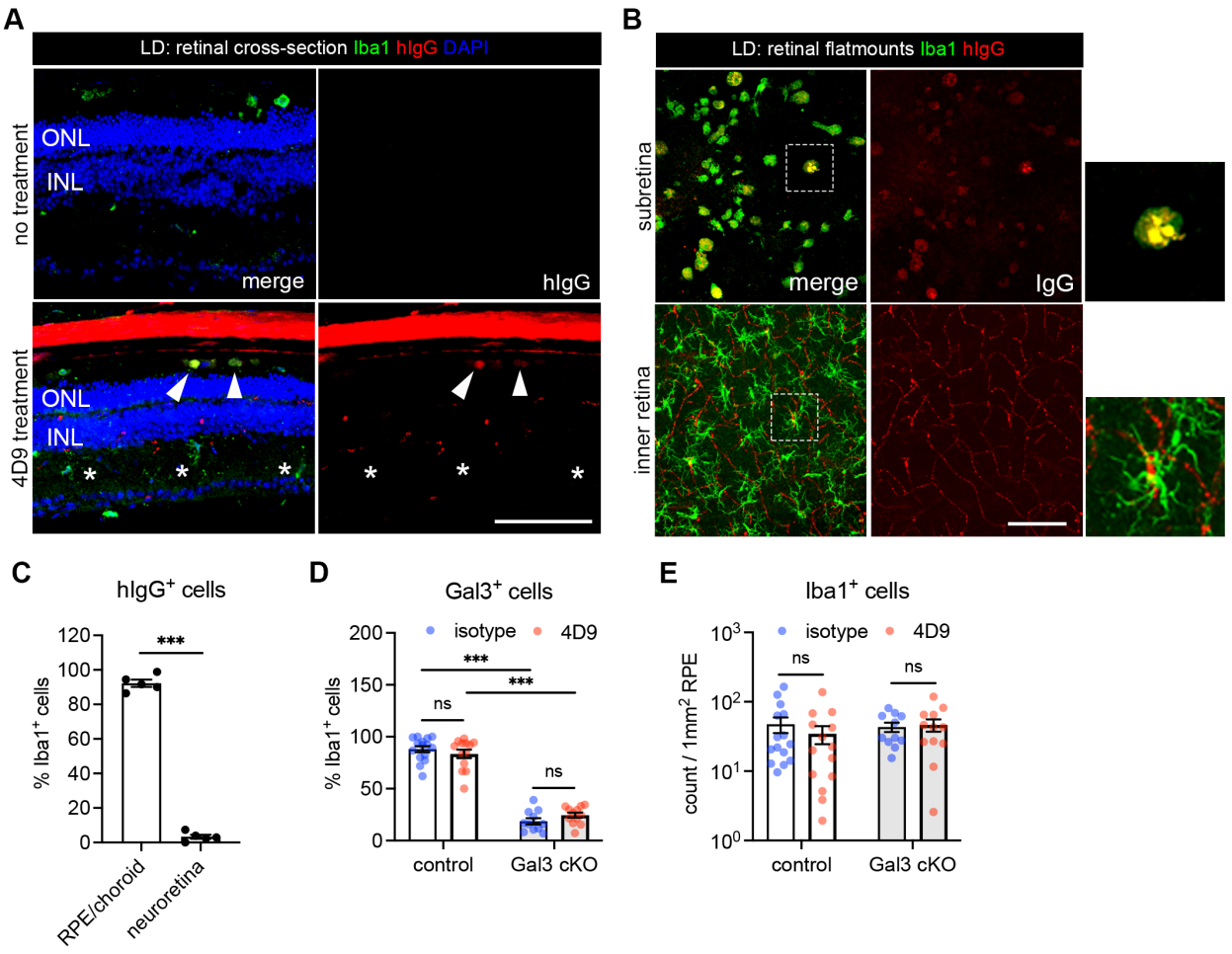

Fig. S4. Subretinal microglia with 4D9 treatment. (**A**) Staining of human IgG (red) and Iba1 (green) in retinal cross sections collected from mice with or without 4D9 treatment in LD. The hIgG is used to trace 4D9 antibodies, which outlines retinal vasculatures in 4D9 treated mice. Arrows indicate the presence of 4D9 antibodies in the subretinal microglia, while asters indicate the absence of 4D9 antibodies in microglia from the inner retina. (**B**) Human IgG (red) and Iba1 (green) staining in RPE and neuroretina flatmounts collected from mice treated with 4D9 antibodies in LD. (**C**) Quantifications of hIgG$^+$ microglia in the subretinal space and neuroretina. (**D** and **E**) Quantifications of Iba1$^+$ cells and Gal3$^+$ cells between control and Gal3 cKO mice treated with either isotype or 4D9 (n=13 per group). Scale bars: 100 μm. Data were collected from 2-4 independent experiments. ***: $p<0.001$; ns: not significant (unpaired Student's t-test: C; two-way ANOVA with Tukey's post hoc test: D and E).

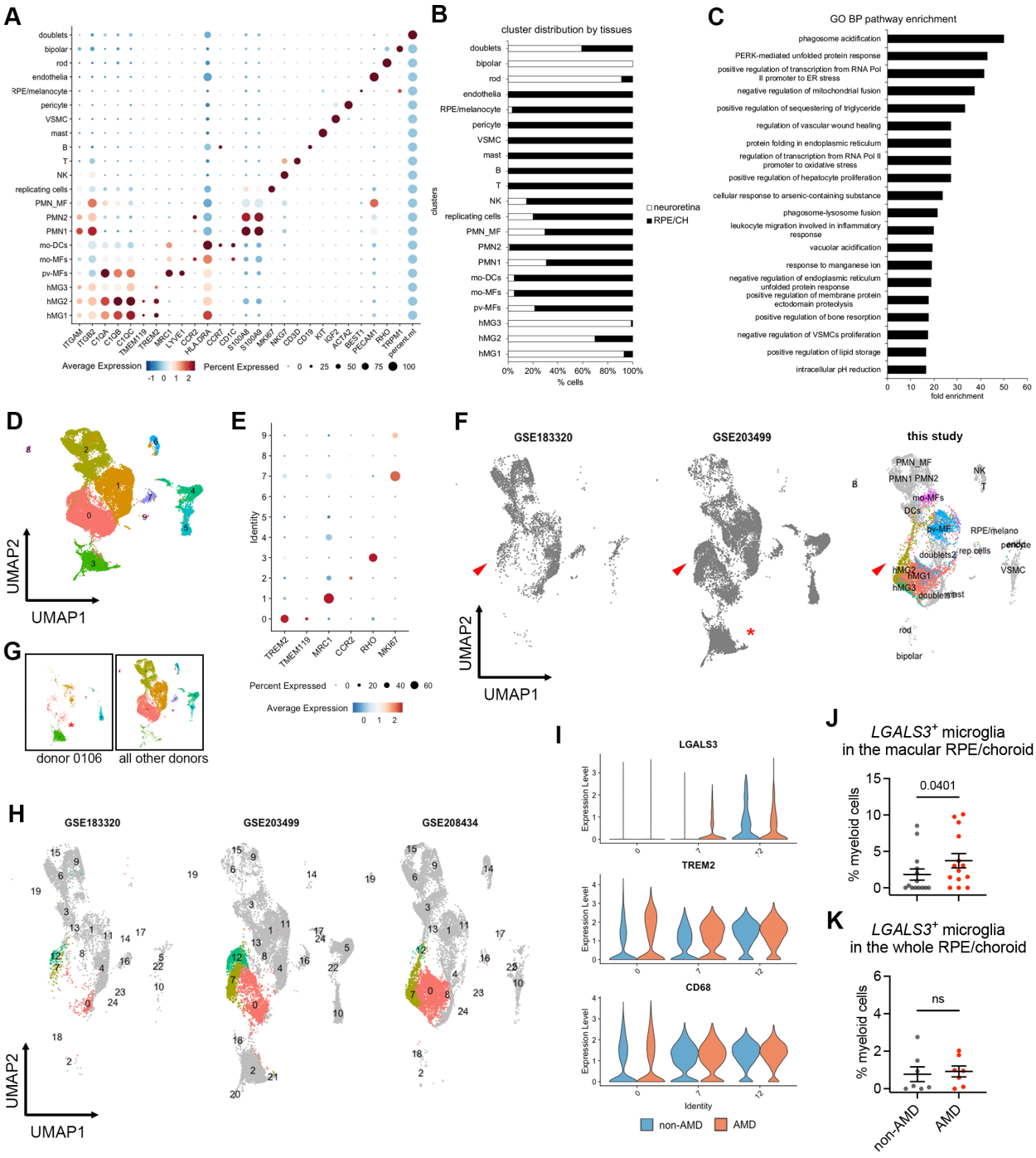

Fig. S5. ScRNA-seq analysis of myeloid cells from human non-AMD and AMD donors. (**A**) Marker expression of all human clusters. hMG, human microglia; mo-MFs, monocyte-derived macrophages; pv-MFs: perivascular macrophages; mo-DCs, monocyte-derived dendritic cells; VSMC, vascular smooth muscle cells. (**B**) Distribution of clusters by neuroretina and RPE/choroid tissues. Cell number of clusters was normalized to the total counts per tissue. (**C**) Pathway enrichment analysis of subretinal microglia with top 200 shared up-regulated genes.

Top significant pathways sorted by false discovery and ranked by fold enrichment are shown. (**D**) UMAP plot showing integrated clustering analysis of three independent human AMD datasets. Data are shown with low resolution to reveal major cell types. (**E**) Dot plot showing the marker expression of major macrophage clusters. Cluster 3 is enriched with *RHO* expression. (**F**) UMAP plots showing the presence of hMG2 cluster in all three scRNA-seq datasets as indicated by arrows. (**G**) UMAP plots showing the enrichment of cluster 3 in donor 0106_nAMD. (**H**) UMAP plots showing clustering analysis with high resolution by each dataset and comparable heterogeneity of microglia (cluster 0, 7 and 12). As dataset GSE183320 does not contain neurosensory retina tissues, few cells of major homeostatic microglia (cluster 0) are observed in this dataset. (**I**) Violin plots showing the expression of *LGALS3*, *TREM2* and *CD68* by microglial clusters between non-AMD and AMD donors. Both cluster 7 and 12 show *LGALS3* upregulation as hMG2 cluster identified in this study. (**J** and **K**) Quantifications of $LGALS3^{+}$ microglial clusters (7 and 12) in the macular and whole RPE/choroid tissues between non-AMD and AMD donors. Data were from three independent datasets and compared using Mann-Whitney test. P-values are shown. ns: not significant.

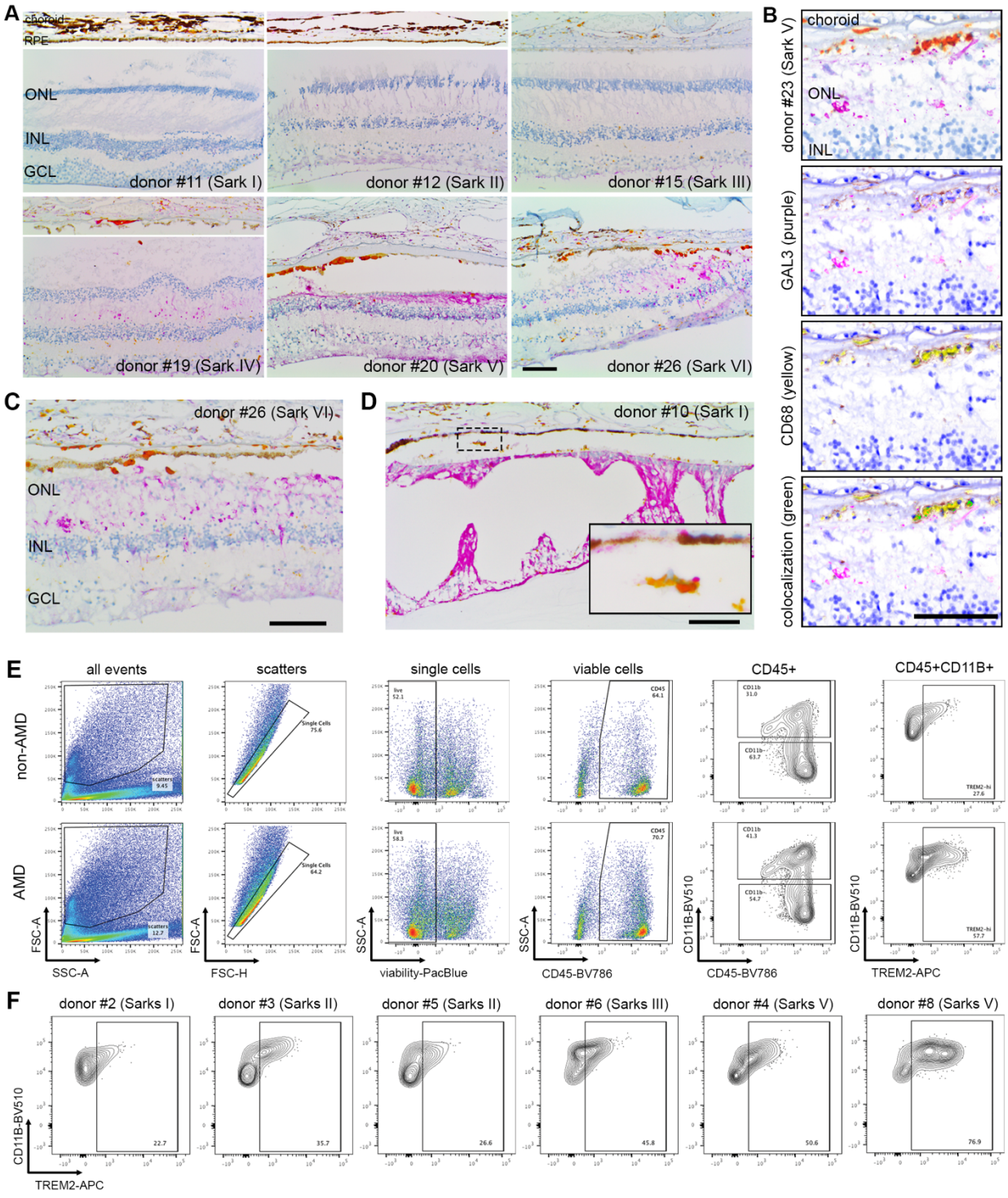

Fig. S6. Validation of GAL3 and TREM2 expression by subretinal myeloid cells in human AMD. (**A**) Images of GAL3 (purple) and CD68 (yellow) co-staining in the macula region of retinal sections from human donors categorized by Sark grades (I-VI). The macular neurosensory retinas of some subject eyes exhibited fixation-related artifactual detachment. In these subjects,

separate images of RPE/choroid tissues are shown. Scale bar: 100µm. ONL and INL, outer and inner nuclear layers. GCL, ganglion cell layer. (**B**) Spectral imaging of GAL3 and CD68 co-staining in the geographic atrophy from donor #23 with advanced AMD (Sarks V). Unmixed purple spectrum (GAL3) and yellow spectrum (CD68) are shown. The areas of colocalized spectra are highlighted in green. Scale bar: 50µm. (**C** and **D**) Images showing the presence of subretinal GAL3 (purple) and CD68 (yellow) double positive cells in the areas with photoreceptor loss and preserved RPE in the transitional area of the macula from an AMD donor (C) and in the age-related peripheral degeneration of a non-AMD donor (D). Scale bars: 100µm. (**E**) Gating strategy of flow cytometry analysis. $CD45^{+}CD11B^{+}$ cells and $CD45^{+}CD11B^{-}$ cells from control blood were used to determine the gating of $TREM2^{+}$ cells. Concatenated plots are shown for non-AMD and AMD. (**F**) Flow contour plots of individual donors showing increased percentage of $TREM2^{+}$ myeloid cells in AMD.